

# Mechanism of Singlet-like Vector Lepton Production and Higgs Autocoupling in Future Positive-negative Electric Lepton Colliders

Wenrong Sun<sup>1\*</sup>

1. School of Science, Department of Physics, The Hong Kong University of Science and Technology, Hong Kong, 999077, China

wsunam@connect.ust.hk

**Abstract:** This paper explores the production mechanism of the singlet vector lepton (VLL) and the Higgs self-interaction based on the theoretical and computational foundations related to the Higgs (Higgs) boson using the future positive-negative electronegative lepton collider (ILC). The way in which VLLs and Higgs are found at the ILC and the role of the Higgs self-coupling strength for the Higgs potential are discussed. Finally two sets of experimental tests are done for validation. One set simulates finding the VLL under the ILC collider and one set tests the accuracy of the Higgs coupling at the ILC collider. The explorations and calculations show that the strength of the Higgs self-coupling is decisive for the Higgs potential. The light subchannel can be excluded from the  $m_{\tau^\pm} \in [180\text{GeV}, 240\text{GeV}]$  integral luminosity when the ILC is  $\sqrt{S} = 500\text{GeV}$  and the integral luminosity  $L \in [3.0\text{fb}^{-1}, 14.9\text{fb}^{-1}]$ .

For the  $e^+e^- \rightarrow HZZ$ -process, when  $n=3, m_H=115\text{GeV}, \sqrt{s}=3.5\text{TeV}, M_S$  the upper limit is  $5\sigma$  found in the unpolarized and +- polarization, where  $P_{e^+} = 0.6, P_{e^-} = 0.8$  it is able to reach 9.75 TeV and 10.1 TeV, respectively. positively and negatively polarized linearly colliding beams can make a significant increase in the extra dimensional effect of the  $e^+e^- \rightarrow HZZ$ -process. It is more efficient to exclude and find the monomorphic VLL and even Higgs through the full hadron channel of the LC.

**Keywords:** ILC collider; singlet vector leptons; Higgs boson; self-coupling

## 1. Introduction

The Standard Model (SM) of particle physics is a quantum field theory that describes known elementary particles and their interactions. The predictions of the SM have been tested experimentally with high precision. However, the SM does not explain several observed results, such as the existence of dark matter, dark energy and the asymmetry of baryons in the universe. In addition, there are theoretical issues such as the hierarchy problem that suggest the need to extend the SM to provide a more complete description of nature [1]. The Large Hadron Collider (LHC) has explored new physics beyond the Standard Model (BSM) at a center of mass energy of  $\sqrt{s} = 13$  TeV. After the discovery of the Higgs scalar boson in 2012 with a mass close to  $M_h=125$  GeV, experimental data from the LHC was found to be consistent with the Standard Model predictions, thus pushing the new particles predicted by new physics to the TeV scale. Many new physics models have been proposed on top of the Standard Model, such as supersymmetric models that degenerate to the Standard Model at low energies. In addition to this, there is a class of new physics models that are based on the Standard Model for the expansion of the fourth generation of chiral fermions, which require the production of large chiral fermion masses through the Yukawa coupling and the Higgs mechanism, and they contribute more to the electroweak precision measurements as well as to the production and decay of the Higgs boson, in contradiction to the experimental data, but if the new fermions are in the Lagrangian equations completely or mostly gain mass in the form of bare electric weak monomorphs, rather than through Yukawa coupling to the Higgs field, then such fermions may exist, and they are vector-like fermions (vectors) [2]. One class of particles couples non-chiral singlet fermions to Standard Model leptons, which are called vector-like leptons (VLL). Many new physics models usually contain vector-like fermions, but they are proposed for other reasons, such as the need for dark matter candidate particles in cosmology and astrophysics, or to solve the hierarchy problem [3]. For example, in supersymmetric models, the supersymmetric model can be minimally expanded with vector-like fermions, and vector-like fermions can lift the lightest Higgs boson mass, enabling the

acquisition of  $M_h = 125$  GeV Standard Model-like Higgs particles at lower supersymmetry-breaking scales, e.g., in the canonically induced supersymmetry-breaking minimal vector-like fermion expansion model, class vector fermions may be found at the LHC [4].

On July 4, 2012, the ATLAS and CMS experimental groups at the LHC jointly announced the discovery of a new boson. The experimental data so far show that the properties of this new particle are compatible with the Standard Model Higgs particle [5]. However, in order to determine whether this particle is a Standard Model Higgs, we need more measurements to determine its properties such as the umlauts, spins, and couplings. At present, the results of all high-energy physics experiments show no signs of significantly exceeding the predictions of the Standard Model, which has been a great success. However, the Standard Model has obvious flaws, and numerous new physics models such as the minimal supersymmetric model and the double Higgs duality model have been proposed. With the obvious flaws of the Standard Model, experimental tests of the coupling properties of Higgs particles have become an important direction in the search for new physics. Among them, the Higgs self-coupling is an indispensable part of understanding the electroweak symmetry spontaneous breaking mechanism and the Higgs mechanism, so the experimental test of the Higgs self-coupling is extremely important. And the experimental test of triple Higgs self-coupling must be carried out through the double Higgs generation process [6].

Existing literature shows that single-state VLLs are difficult to discover in future hadron colliders and face great challenges. Literature [7] studies the topic of finding VLL in the half-photon channel of the high-energy  $e^- + e^-$  collider, based on the different decay modes of the electroweak standard boson, the signal is divided into two modes, A and B, and detailed detector simulations are carried out respectively, and it is found that the A mode is more capable of ruling out and discovering the VLL. Literature [8] proposes that the construction of new particles that go beyond the Standard Model is an important exploration of the new physics beyond the Standard Model as a via. Vector-like leptons have attracted much attention in both experiment and theory. Finally, the research prospect of searching for heavy state VII in the field of pure lepton channel

and all-hadron channel is explored. Literature [9] studies a simplest feasible dark matter model with a real single heavy state scalar, vector-like single heavy state and double state leptons. The Large Hadron Collider (LHC) observes new fermion sector double lepton production and exhibits ET features. A minimal extension of the Standard Model (SM) including a supercharged scalar triplet and two vector-like leptons, a doublet and a singlet, has been proposed in the literature [10] to account for both the non-zero neutrino mass and the dark matter (DM) content of the universe. DM cannot be detected at colliders while the charged partners of DM can produce large displacements at the Large Hadron Collider.

Higgs' self-coupling is an integral part of understanding the electroweak symmetry spontaneous breaking mechanism and the Higgs mechanism. A multivariate analysis of the production of the Higgs self-coupling (THSC)  $\lambda 3H$  in the HL-LHC  $HH \rightarrow b\bar{b}\gamma\gamma$  channel has been carried out in the literature [11], where we employed the state-of-the-art event generator of POWHEG-BOX-V2 to exploit the next-to-leading-order (NLO) distribution of the multivariate data analysis (TMVA) toolkit to process the signal, and, taking into account the top-quark mass as a case study, took a  $\lambda 3H=1$  trained augmented decision tree (BDT) analysis is found to be significant up to 1.95 for about nine signals and ten background event conditions. The literature [12] explores the effect on the sensitivity of the Higgs self-coupling  $\lambda$  in the case of two Higgs bosons produced by vector boson scattering at the LHC. In order to predict the sensitivity of this coupling, the value of  $\lambda$  is probed and quantified by investigating the role of  $\lambda$  at the level of sub-processes through the process of vector boson scattering in the LHC. In the literature [13] the dominant two-loop corrections to the Higgs trilinear coupling and the Higgs quadratic coupling in the extended Higgs sector model were computed using the eigenpotential approximation. The results are obtained by analyzing three beyond Standard Model scenarios, based on which the contribution and influence of the two-loop BSM on the Higgs self-coupling are investigated. The size of the two-loop corrections is found to be much smaller than the size of the one-loop corrections under fine-tuning conditions.

In this paper, firstly, the differences between the Higgs boson and the Standard Model are sorted out, and the formula for the Higgs boson is sorted out. Secondly, the ILC collider is chosen to detect VLLs as well as Higgs particles, in order to solve the problem that the singlet VLLs are difficult to be found in hadron colliders. On this basis, the focus is on probing the algorithm of Higgs self-interaction and the effect of intensity on the Higgs potential. Finally two sets of tests are done. One set tests the prospects of finding VLLs as well as Higgs through the pure lepton channel, the full hadron channel, and the semi-lepton channel at the  $e^+e^-$  collider based on the above formulas. The other set of tests investigates Higgs self-coupling through  $e^+e^- \rightarrow HZZ$  this process, testing the extra dimensional effects for different positive and negative electron polarization states. The tests show that the pure lepton channel process requires a much brighter integral brightness to rule out or find VLLs compared to the full hadron channel. The accuracy of detecting extra dimensions will be greatly improved with positive and negative polarization of the beam current.

## 2. Future Positive and Negative Electro-Lepton Collider

### 2.1 Computational basis of Higgs boson correlation theory

To generate mass for three weak canonical bosons propagating short-range weak interactions in the Standard Model, it is necessary to introduce scalar fields with at least three degrees of freedom. There is then no more economical choice than to introduce a

complex scalar field  $\Phi = \begin{pmatrix} \phi^+ \\ \phi^0 \end{pmatrix}$ , which is the dual state of  $SU(2)$ , supercharged

$Y = +1$ , and therefore  $\phi^+$  charged with  $+e$  and  $\phi^0$  uncharged.  $\Phi$  carries four real degrees of freedom, and the Riesz measure describing this scalar field is expressed as follows:

$$L_H = (D_\mu \Phi)^\dagger (D^\mu \Phi) - V(\Phi^\dagger \Phi) \quad (1)$$

Among them:

$$V(\Phi) = \mu^2 (\Phi^\dagger \Phi) + \frac{\lambda}{4} (\Phi^\dagger \Phi)^2 \quad (2)$$

is the self-interaction potential of the  $\Phi$ -field. In order for there to be a vacuum expectation value, i.e., a minimum, for the interaction potential, there must be a limit of  $\lambda > 0$ . For the square term part, there are two possibilities:

(1)  $\mu^2 > 0$ . the minimum value of the potential energy is 0, i.e.  $\langle 0 | \Phi | 0 \rangle \equiv \Phi_0 = 0$ . the Raschel quantity  $L_H$  will also degenerate into a Raschel quantity of a spin 0 mass  $\mu$  particle which means nothing to us. Therefore this situation does not satisfy our needs.

(2)  $\mu^2 < 0$ . The condition for the existence of a minimum value of potential energy is:

$$\Phi^\dagger \Phi = \frac{v^2}{2}, \quad v = 2\sqrt{\frac{-\mu^2}{\lambda}} \quad (3)$$

As demonstrated in the arithmetic. Since  $\Phi$  is a complex scalar field, it corresponds to an infinite number of vacuum expectation values for a circle in the  $\Phi$  complex plane.

For the second case when we have to choose a vacuum state, the symmetry of the system is broken, i.e. spontaneous symmetry breaking occurs. Considering that the symmetry of  $U(1)_Q$  has to be maintained, the vacuum expectation value of the charged component of  $\Phi$  cannot be zero and the neutral component has to have a non-zero vacuum expectation value. Typically the vacuum expectation value of  $\Phi$  is chosen:

$$\Phi_0 \equiv \langle 0 | \Phi | 0 \rangle = \begin{pmatrix} 0 \\ v \\ \frac{v}{\sqrt{2}} \end{pmatrix} \quad (4)$$

This freedom to choose the vacuum state  $\Phi$  will spontaneously break the  $SU(2)_W \otimes U(1)_Y$ -symmetry to the  $U(1)_Q$ -symmetry of the residual EM. If we separate the vacuum expectation from  $\Phi$ :

$$\Phi = \Phi' + \Phi_0 = \begin{pmatrix} \phi^+ \\ \phi^0 = (v + H + i\chi)/\sqrt{2} \end{pmatrix} \quad (5)$$

Where  $\Phi' \equiv \begin{pmatrix} \phi^+ \\ (H + i\chi)/\sqrt{2} \end{pmatrix}$  is the field  $(\langle|\Phi'|\rangle = 0)$  with vacuum expectation value 0, then  $\Phi$  is parametrized by the real scalar fields  $H$  and  $\chi$ , the complex scalar field  $\phi^+$  and the real positive expectation value  $v$ . We can see that only field  $H$  has been shifted so that the other fields still retain zero mass to become the Goldstone boson while field  $H$  represents the physical Higgs boson. Putting (5) and (6) (where  $I_\Phi^i = \sigma^i / 2$ ,  $Y_\Phi = 1$ ,  $T_{C,\Phi}^a = 0$ ) as well as the redefined canonical fields, the arithmetic is as follows:

$$W_\mu^\pm = \frac{1}{\sqrt{2}}(W_\mu^1 \mp iW_\mu^2), Z_\mu = \frac{gW_\mu^3 - g'B_\mu}{\sqrt{g^2 + g'^2}}, A_\mu = \frac{gW_\mu^3 + g'B_\mu}{\sqrt{g^2 + g'^2}} \quad (6)$$

## 2.2 The ILC collider and its parameters

The ILC collider employs a dual detector design, the SID and ILD detectors. The SID is a general purpose detector designed to make precise measurements at the ILC for Jet energies as well as charged leptons, photons, and lost energies in a particle flow algorithm based approach, which is capable of meeting the challenging requirements of the ILC for a physics detector. The SID is designed with consideration of both the economic costs, and its internal high-performance components are designed to be compact while maintaining critical performance levels. The ILD is a multi-purpose detector that is designed to optimize particle flow performance. The design of the dual detector is inspired by existing collider experiments, where the two detectors are able to complement their own strengths and cross-validate the experimental results obtained. Table 1 shows the detailed parameters of the current mainstream colliders, with  $\sqrt{s}(\text{GeV})$  values roughly in the range of 500, 1000, and 1500.

Table 1 The future line is the basic parameter of the machine

Parameter	TESLA	NLC/JLC	CLIC

$\sqrt{s}$ (GeV)	500	800	500	1000	3000
Gradient (MV/m)	23	35	48	48	150
$L_{cur} (10^{34} \text{ cm}^{-2} \text{ s}^{-1})$	3.4	5.8	2.0	3.4	0
$L_{int} / 10^7 \text{ s} (\text{fb}^{-1})$	340	580	200	340	1000
Beamstrahlung spread (%)	3.2	4.3	4.7	10.2	31

Table 2 shows the physical processes at the collider, showing the main physical processes studied at the ILC collider at different center-of-mass energies and the main physical goals of studying these processes.

Table 2 ILC Major physical processes

Cardiac energy	Decay process	Physical objective
91 GeV	$e + e^- \rightarrow Z$	Super precision power
160 GeV	$e + e^- \rightarrow WW$	Super precision W
250 GeV	$e + e^- \rightarrow Zh$	Precision Higgs coupling
350-400 GeV	$e + e^- \rightarrow t\bar{t}$	Top quark quality and coupling
	$e + e^- \rightarrow WW$	Precision W coupling
	$e + e^- \rightarrow \bar{v}vh$	Precision Higgs coupling
500 GeV	$e + e^- \rightarrow f\bar{f}$	Looking for z
	$e + e^- \rightarrow t\bar{t}h$	The Higgs particle is coupled with the top quark
	$e + e^- \rightarrow Zh$	Higgs coupling
	$e + e^- \rightarrow XX$	Look for supersymmetry
	$e + e^- \rightarrow AH, H^+H^-$	Looking for the higgs extension state
700-1000 GeV	$e + e^- \rightarrow \bar{v}vh$	Higgs coupling
	$e + e^- \rightarrow \bar{v}VV$	Compound higgs region

	$e+e-\rightarrow \bar{v}v\bar{t}t$	Compound higgs particles and top quarks
	$e+e-\rightarrow \bar{t}\bar{t}$	Look for supersymmetry

## 2.3 Mechanism of production of singlet-like vector leptons

The reaction on the ILC is relatively simple, with a well-defined initial state and a relatively simple final state. It has a good signal-to-noise ratio and the very clean experimental environment allows us to easily discover new physical phenomena and perform ultra-high precision studies. Photon-electron collisions are the same as for all other types of quarks and leptons and new particles beyond the Standard Model. Figure 1 shows the Feynman diagram form of the Higgs boson produced on the ILC. The cross sections for annihilation to produce all types, new or exotic pairs of particles are on a similar order of magnitude.

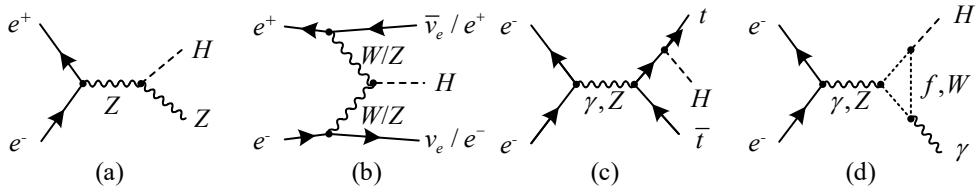


Figure 1 The standard type higgs boson is produced in the electronic collider

The ILC provides a deterministic energy for the center-of-mass system and regulates the polarization of the primordial positron and negative electron. At the LHC, all calculations of scattering cross sections depend on QCD. all theoretical calculations of the signal or background have systematic uncertainties from the PDF, unknown perturbative QCD corrections, and non-perturbative QCD effects. the NLO QCD corrections tend to be at the level of 30-50%. For Higgs boson production, the first corrections are even reachable. In order to obtain theoretical errors smaller than that, it is often necessary to calculate to or now higher orders than can be reached for some of the simplest reactions. On the top, both positive and negative electrons in the initial state are fundamental point particles and are only involved in electroweak interactions. The first time for the scattering cross section is often only at the level of a few percent, and a little effort can lead to theoretical accuracies of a few thousandths of a percent.

The degree of importance of the individual Higgs production processes at the  $e^+e^-$  collider is closely related to the center-of-mass system energy and, in some regions, to the Higgs boson mass. A typical Feynman diagram of the lowest order for the main Higgs production processes at the  $e^+e^-$  collider is given in Fig. 1. In the LEP energy region ( $\sqrt{s} = 209\text{GeV}$ ), the production of  $e^+e^- \rightarrow Z^* \rightarrow ZH$  by "Higgs radiation" of  $ZH$  is the dominant process. Due to the extremely small electron Yukawa coupling, the  $H\gamma$  production process at the lowest order is dominated by the exchange of heavy fermion loops and  $W$  boson loops, and thus the scattering cross section is relatively low. Nevertheless, some instances can be expected to be detected. At the ILC in the pipeline, the three additional production channels become increasingly important.  $W$ -boson convergence  $e^+e^- \rightarrow W^{+\ast}W^{-\ast}\nu\bar{\nu} \rightarrow H\nu\bar{\nu}$ ,  $Z$ -boson convergence  $e^+e^- \rightarrow Z^*Z^*e^+e^- \rightarrow He^+e^-$  and the Higgs boson accompanied by top-quark pair production  $e^+e^- \rightarrow Ht\bar{t}$ .

Since  $ZH$  generation is similar to a  $s$ -channel process, the scattering cross section can reach a maximum just above the threshold and then decline roughly in the form of  $1/s$ , as in a typical  $s$ -channel process. In contrast, the  $W/Z$ -aggregation process, which is similar to the  $t$ -channel process, increases incrementally with energy in a form similar to  $\ln(s/M_H^2)/M_W^2$ . Above the threshold ( $\sqrt{s} > 2m_t + M_H$ ) for  $Ht\bar{t}$  production, Higgs accompanied by top-quark pair production offers the possibility of direct measurements of 10 quark Yukawa couplings with high precision.

## 2.4 Higgs self-coupling study

Figure 2 shows the process of Higgs boson pair production on the ILC with respect to the strength of the cubic Higgs self-coupling. The cross-section of Higgs boson pair production in the SM is very small, but the process is very important, especially because its precise measurement contributes to the understanding of the strength of the cubic Higgs coupling in the SM. Such a restriction is more stringent for many new physics models beyond the SM, and thus the experimental search for the production of Higgs boson pairs never stops. At the same time the self-coupling strength has a very intuitive

effect on the shape of the Higgs potential, so understanding the self-coupling strength will also refresh the understanding of the electroweak phase transition. The cross section of the Feynman diagram associated with the four Higgs self-coupling strengths is very small, and the three Higgs end states are more complex, making measurements at modern colliders even more difficult. Experimental measurements at higher energies, higher luminosities, or at future colliders of the Positron-Negative Electron Collider (PNEC) with cleaner backgrounds are needed.

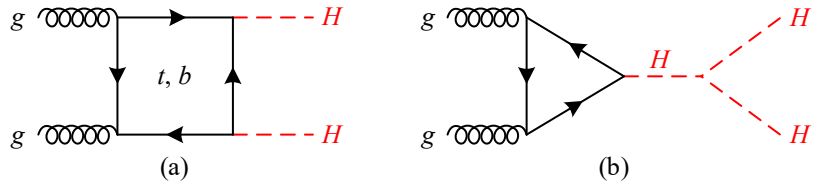


Figure 2 Higgs self-interaction

The (a) quark loop in figure (2) accounts for the most dominant contribution, while the (b) contribution in figure 2 is smaller, but when the modulo-square operation is performed with figure 2(a) the result is smaller than that of considering only the single figure 2(a). From the Feynman diagrams, it is clear that only Fig. 2(b) is related to the strength of the cubic Higgs coupling, so experimental measurements of the strength of the cubic Higgs coupling need to exclude the contribution from Fig. 2(a). This requires more accurate Yukawa coupling constants for Top and Bottom quarks. The current latest experimental limits are from ATLAS at 95% confidence level  $-5.0 < k_\lambda < 12$  and CMS at 95% confidence level  $-11.8 < k_\lambda < 18.8$ . where  $k_\lambda$  is the ratio of the Higgs self-coupling strength beyond the SM to the self-coupling strength in the SM. With the accumulation of experimental data, a tighter limit on  $k_\lambda$  will be imposed in the future. The uncertainty in the results of the three Higgs self-coupling strengths on the experiments is still large, and the Higgs self-coupling strength plays a decisive role in the shape of the Higgs potential.

The standard model Higgs potential is as follows:

$$V(\Phi) = -\mu^2 (\Phi^\dagger \Phi) + \frac{\lambda}{4} (\Phi^\dagger \Phi)^2 \quad (7)$$

Expand  $\frac{\lambda}{4}(\Phi^\dagger\Phi)^2$  of them:

$$\frac{\lambda}{4}(\Phi^\dagger\Phi)^2 = \frac{\lambda v}{4} H^3 + \frac{\lambda}{16} H^4 + \dots \quad (8)$$

It can be seen that three-Higgs self-coupling and four-Higgs self-coupling vertices occur in the standard model.

Higgs self-coupling in the double Higgs dual state model. For the double Higgs dual state model, the Higgs potential is as follows:

$$\begin{aligned} V(\Phi_1, \Phi_2) = & m_{11}^2 \Phi_1^\dagger \Phi_1 + m_{22}^2 \Phi_2^\dagger \Phi_2 + \frac{\lambda_1}{2} (\Phi_1^\dagger \Phi_1)^2 + \frac{\lambda_2}{2} (\Phi_2^\dagger \Phi_2)^2 \\ & + \lambda_3 (\Phi_1^\dagger \Phi_1)(\Phi_2^\dagger \Phi_2) + \lambda_4 (\Phi_1^\dagger \Phi_2)(\Phi_2^\dagger \Phi_1) \\ & + \frac{\lambda_5}{2} \left[ (\Phi_1^\dagger \Phi_2)^2 + (\Phi_2^\dagger \Phi_1)^2 \right] \end{aligned} \quad (9)$$

All terms except the mass term contribute to the Higgs self-coupling, but of course we are discussing Higgs potentials that satisfy  $Z_2$ -symmetry and CP conservation, and generalized Higgs potentials contain more terms, making the Higgs self-coupling more complicated. As in the Standard Model, vertices with three-Higgs and four-Higgs couplings occur in the dual Higgs dual model. In the double Higgs dual state model, due to the presence of two Higgs dual states, there are five physical Higgs fields:

$H^0, h^0, A^0$  and  $H^\pm$ . There are many different kinds of couplings between the five physical Higgs fields, and in Table 3 we give all the combinations of couplings between the Higgs fields.

Table 3 Higgs boson interaction

Particles	Vertices	Particles	Vertices
$HHH$	$i \left[ -\frac{3M_H^2}{v} + \frac{33x^2 M_H^2 v}{4f^2(1-x^2)} \right]$	$HH\Phi^0$	$iM_\Phi^2 v' \left( \frac{29\sqrt{2}}{3f^2} + \frac{2\sqrt{2}}{v^2} \right)$
$H\Phi^0\Phi^0$	$iM_\Phi^2 \left( \frac{4v}{3f^2} - \frac{16v'^2}{v^3} - \frac{60v'^2}{f^2 v} \right)$	$HG^0 G^0$	$i \left[ -\frac{M_H^2}{v} + \frac{11x^2 M_H^2 v}{4f^2(1-x^2)} \right]$
$H\Phi^P\Phi^P$	$iM_\Phi^2 \left( \frac{4v}{3f^2} - \frac{16v'^2}{v^3} - \frac{20v'^2}{f^2 v} \right)$	$HG^0 \Phi^P$	$iM_\Phi^2 v' \left( \frac{11\sqrt{2}}{3f^2} + \frac{2\sqrt{2}}{v^2} \right)$

$H\Phi^+\Phi^-$	$iM_\Phi^2 \left( \frac{2v}{3f^2} - \frac{8v'^2}{v^3} - \frac{46v'^2}{3f^2v} \right)$	$HG^+G^-$	$i \left[ -\frac{M_H^2}{v} + \frac{11x^2M_H^2v}{6f^2(1-x^2)} \right]$
$H\Phi^+G^-$	$iM_\Phi^2 v' \left( \frac{13}{3f^2} + \frac{2}{v^2} \right)$	$\Phi^0\Phi^0\Phi^0$	$-i \frac{8\sqrt{2}M_\Phi^2 v'}{f^2}$
$\Phi^0\Phi^P\Phi^P$	$-i \frac{8\sqrt{2}M_\Phi^2 v'}{3f^2}$	$\Phi^0G^0G^0$	$iM_\Phi^2 v' \left( \frac{7\sqrt{2}}{3f^2} - \frac{2\sqrt{2}}{v^2} \right)$
$\Phi^0\Phi^PG^0$	$-i \frac{2M_\Phi^2 v'^2}{f^2 v}$	$\Phi^0G^+G^-$	$i \frac{7\sqrt{2}M_\Phi^2 v'}{3f^2}$
$\Phi^0\Phi^+\Phi^-$	$-i \frac{8\sqrt{2}M_\Phi^2 v'}{3f^2}$	$\Phi^0\Phi^+G^-$	$iM_\Phi^2 \left( \frac{\sqrt{2}v}{3f^2} - \frac{4\sqrt{2}v^2}{v^3} - \frac{10\sqrt{2}v^2}{f^2v} \right)$

### 3. Experimentation and analysis

#### 3.1 Single-state vector-like lepton generation and detection experiments

The following colliders will be selected for this experiment:

ILC with highest integral luminosity  $4ab^{-1}$  and center-of-mass energy  $\sqrt{S} = 500Gev.$

ILC with highest integral luminosity  $8ab^{-1}$ , center-of-mass energy  $\sqrt{S} = 1000Gev.$

ILC with highest integral luminosity  $3.5ab^{-1}$  and center of mass energy  $\sqrt{S} = 1500Gev.$

According to the performance of the collider, the polarization is analyzed and the appropriate polarization is selected to increase the cross section size of the signal, then the signal is analyzed and the examples of the signal and background processes are generated using the relevant procedures, in which the signal is classified into three cases, the pure lepton channel, the full hadronic channel and the semi-lepton channel, which

are discussed and analyzed separately, and the final conclusions of the study are given. In this paper only the computational procedure for pure leptonic channel is shown.

Figure 3 shows the different electron scattering cross sections, demonstrating,  $e^+e^- \rightarrow \tau' + \tau' -$  the magnitude of the scattering cross section when different electron polarizations  $P_{e^-}$  and  $P_{e^+}$  are taken for cases  $m_{\tau'} = 200\text{GeV}$  and  $\sqrt{s} = 500\text{GeV}$ , where the contour lines represent the magnitude of the scattering cross section in units of  $\text{fb}$ . We can see that the symmetry centroid of the contour lines is nearer to  $(P_{e^-} = -0.6, P_{e^+} = +0.6)$  rather than  $(P_{e^-} = 0, P_{e^+} = 0)$ , which is caused by the  $Z$  boson acting as a propagator during the  $e^+e^- \rightarrow \tau'\tau' -$  process. The polarization cross section tends to be maximum when  $P_{e^-} \rightarrow 1, P_{e^+} \rightarrow -1$  this is due to the fact that the  $e^+e^- \rightarrow \tau'\tau' -$  polarization cross section  $\sigma_{P_{e^-}P_{e^+}}$  can be written as,

$$\sigma_{P_{e^-}P_{e^+}} = (1 - P_{e^-}P_{e^+})\sigma_0(1 - P_{\text{eff}}A_{LR}) \quad (10)$$

In which

$$\sigma_0 = \frac{\sigma_{RL} + \sigma_{LR}}{4} \quad (11)$$

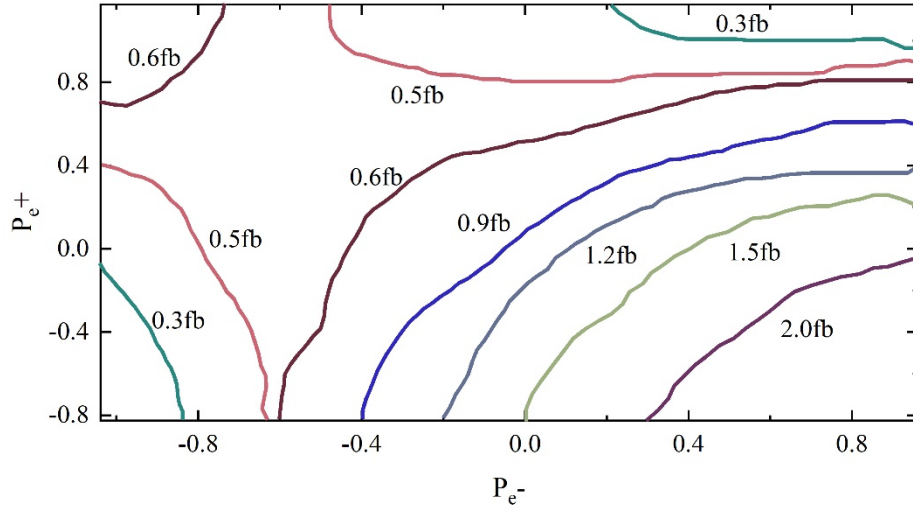


Figure 3 The scattering cross section of electrons when different

The specific expression of the unpolarized cross section is given in the following equation:

$$A_{LR} = \frac{\sigma_{LR} - \sigma_{RL}}{\sigma_{LR} + \sigma_{RL}} \quad (12)$$

Representing left-right asymmetry and there:

$$P_{eff} = \frac{P_{e^-} - P_{e^+}}{1 - P_{e^-} P_{e^+}} \quad (13)$$

Represents the effective polarization,  $\sigma_{RL}$  is the scattering cross section for the fully right-handed polarized  $e^-$  beam ( $P_{e^-} = +1$ ) and the fully left-handed polarized  $e^+$  beam ( $P_{e^+} = -1$ ), and the scattering cross section  $\sigma_{LR}$  is defined similarly. In principle, only the electron beam needs to be polarized, however, even a small polarization of the positron beam can increase the effective polarization. A 70% polarization of the electron beam and a -40% polarization of the positron beam can yield almost 80% of the effective initial polarization. Considering the limitations of the prior art, we chose the following polarization in our calculations:

For  $\sqrt{s} = 500\text{GeV}$ ,  $P_{e^-} = 0.8$ ,  $P_{e^+} = -0.3$ .

For  $\sqrt{s} = 1000\text{GeV}$ ,  $P_{e^-} = 0.8$ ,  $P_{e^+} = -0.2$ .

For  $\sqrt{s} = 1500\text{GeV}$ ,  $P_{e^-} = 0.8$ ,  $P_{e^+} = 0$ .

Figure 4 illustrates the left-right asymmetry factor  $A_{LR}$  as a function of  $m_{\tau'^{\pm}}$  for  $\sqrt{s} = 500\text{GeV}$ ,  $1000\text{GeV}$  and  $1500\text{GeV}$ . It can be seen that the value of  $A_{LR}$  can reach -70%, which means that the  $Z$  boson induces a chiral destruction effect.

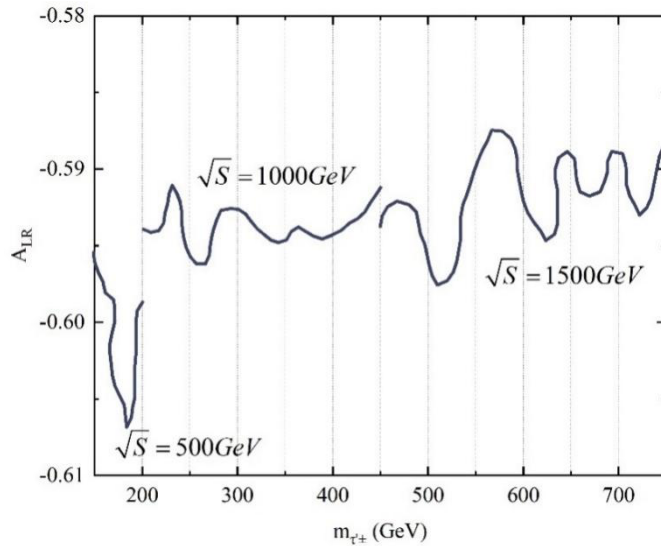


Figure 4 The relationship between the function of the factor in the different gev

Three decay modes are selected for the signal, i.e., pure light subchannel, full-strength subchannel, and half-light subchannel, and the signal is generated and decayed as shown below:

Pure Lightning Son said:  $e^+e^- \rightarrow \tau' + \tau' \rightarrow (W^+\bar{V}_\tau)(\tau^-Z) \rightarrow (\ell^+\nu_e\bar{V}_\tau)(\tau^-\ell^+\ell^-)$ .

All Johnnie said:  $e^+e^- \rightarrow \tau' + \tau' \rightarrow (W^+\bar{V}_\tau)(\tau^-Z) \rightarrow (jj\bar{V}_\tau)(\tau^-jj)$ .

Semi-leptonic path model A:  $e^+e^- \rightarrow \tau' + \tau'^- \rightarrow (W^+\bar{V}_\tau)(\tau^-Z) \rightarrow (\ell^+\nu_e\bar{V}_\tau)(\tau^-jj)$ .

Semi-Lightweight Subtract Mode B:  $e^+e^- \rightarrow \tau' + \tau'^- \rightarrow (W^+\bar{V}_\tau)(\tau^-Z) \rightarrow (jj\bar{V}_\tau)(\tau^-\ell^+\ell^-)$ .

Based on these signal characteristics, we analyze the main background of the Standard Model process  $\tau^+\tau^-$ ,  $ZZ$ ,  $Zh$ ,  $ZW^+W^-$ ,  $t\bar{t}Z$ , and  $ZZZ$ . To perform the simulation calculations, we implement the monostatic VLL model into the FeynRules package, generating model files in UFO format. We then used MG5\_aMC to calculate the scattering cross-section sizes after the signal and background decays and display the results in Table X. The results are shown in Table X. Some of the sub-instances of the signal and background need to pass the basic screening, as shown below:

$$\begin{aligned} \Delta R(x, y) &> 0.4, & x, y = L(\ell, \tau), j(g, u, d, c, s), b \\ p_T^L &> 10 \text{ GeV}, & |\eta_L| < 2.5 \\ p_T^b &> 20 \text{ GeV}, & |\eta_b| < 2.5 \\ p_T^j &> 20 \text{ GeV}, & |\eta_j| < 5.0 \end{aligned} \quad (14)$$

where  $p_T$  is the transverse HO momentum, while  $\Delta R(x, y) = \sqrt{(\Delta\phi)^2 + (\Delta\eta)^2}$ ,  $\Delta\phi$  are the difference in azimuth between  $x$  and  $y$ , and  $\Delta\eta$  is the difference in pseudo-rapidity between them. These basic filters are used to model the geometrical acceptance of the detector and the detection threshold.

Considering the limitations of current experiments and collision energies, the parameter space is chosen as follows:

$$m_{\tau'^\pm} \in [180, 250] \text{ GeV}, \sqrt{s} = 500 \text{ GeV}.$$

$$m_{\tau'^\pm} \in [240, 500] \text{ GeV}, \sqrt{s} = 1000 \text{ GeV}.$$

$$m_{\tau^{\pm}} \in [450, 750] \text{GeV}, \sqrt{s} = 1500 \text{GeV}.$$

And pick three basic points:

$$m_{\tau^{\pm}} = 200 \text{GeV}, \sqrt{s} = 500 \text{GeV}.$$

$$m_{\tau^{\pm}} = 350 \text{GeV}, \sqrt{s} = 1000 \text{GeV}.$$

The relevant input parameters for the standard model are as follows:

$$\begin{aligned} m_t &= 173.0 \text{GeV}, m_Z = 91.1876 \text{Gev}, m_h = 125 \text{GeV}, \\ \sin^2 \theta_w &= 0.231, \alpha(m_z) = 1/128.877 \end{aligned} \quad (15)$$

In Fig. 5 demonstrates the signal interface size at  $\sqrt{S}$ , 350, and 600 GeV versus  $\sqrt{S}$ . The scattering cross-section size increases sharply with the center-of-mass energy  $\sqrt{S}$  first, and then starts to decrease gradually after reaching the highest point, which is due to the depressing of the center-of-mass energy during  $s$ -channel generation.

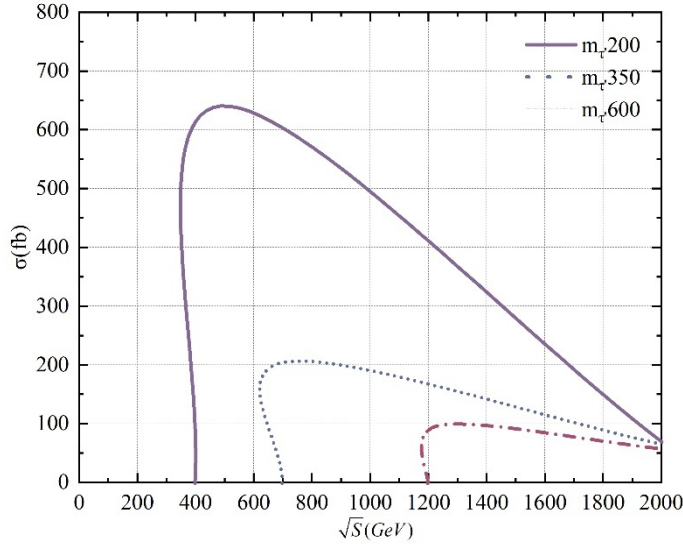


Figure 5 Signal cross section

Figure 6 shows the relationship between the size of the cross section and  $\sqrt{S}$  after the decay of the signal and background processes at time  $m_{\tau^{\pm}} = 200 \text{GeV}$ . The cross sections of the backgrounds  $\sqrt{S} = 1000 \text{GeV}$ , ZZ, and Zh are all larger than the signal, while the main background is about 1000 times larger than the signal, in order to increase the significance of the signal. The instances generated by MG5, parton levels

are passed to Pythia for parton clustering and hadronization, and then Delphes is used to do fast detector simulations, and for jet injection is processed using the *anti-kt* algorithm, where the distance parameter  $\Delta R = 0.5$ .

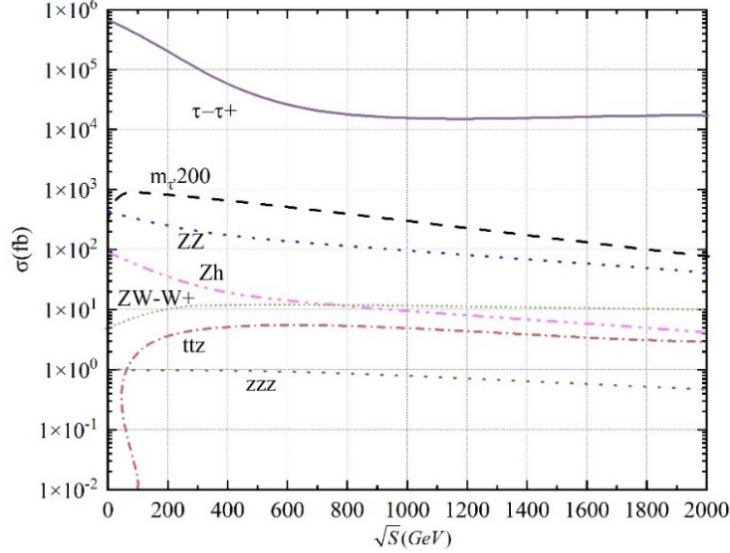


Figure 6 The relationship between the signal process and the size of the cross section

The background  $\tau^+\tau^-$  is approximately 1000 times larger than the signal. In order to improve the significance of the signal, it is necessary to perform detailed detector simulations and select some effective cuts to suppress these backgrounds. In the detector simulation of the final state, the instances generated by MG5 are passed to Pythia6 for partial subcluster injection and hadronization, and then fast detector simulation is done with Delphes, and for jet injection is handled using Fastjet and *anti-kt* algorithms, where the distance parameter  $\Delta R = 0.5$ . Finally the analysis was performed using MadAnalysis5. Table 4 shows the process of signal and background in the experiment.

Table 4 Pure light channel citic and the background process

	Process	Scattering section (fb)		Pure light child decay mode
		$m_\tau 200 \sqrt{s} = 500$ (GeV)	$m_\tau 350 \sqrt{s} = 1000$ (GeV)	

Signal	$e^+e^- \rightarrow \tau'^+\tau'^-$	2.644	0.576	$(\tau' \rightarrow W^+\bar{\nu}_\tau, W^+ \rightarrow \ell^+\nu_\ell),$ $(\tau' \rightarrow \tau^-Z, Z \rightarrow \ell^+\ell^-)$
Back drop	$e^+e^- \rightarrow \tau^+\tau^-$	474.4	110.9	
	$e^+e^- \rightarrow ZZ$	10..9	2.373	$Z \rightarrow L^-L^+, Z \rightarrow \nu_\ell\bar{\nu}_\ell$
	$e^+e^- \rightarrow Zh$	5.572	0.923	$Z \rightarrow L^-L^+, h \rightarrow all$
	$e^+e^- \rightarrow ZW^+W^-$	0.057	0.071	$Z \rightarrow L^-L^+, W^+ \rightarrow L^+\nu_\ell,$ $W^- \rightarrow L^-\bar{\nu}_\ell$
	$e^+e^- \rightarrow t\bar{t}Z$	0.0043	0.016	$(t \rightarrow W^+b, W^+ \rightarrow L^+\nu_\ell),$ $(\bar{t} \rightarrow W^-\bar{b}, W^- \rightarrow L^-\bar{\nu}_\ell),$ $Z \rightarrow L^-L^+$
	$e^+e^- \rightarrow ZZZ$	0.0039	0.0025	$Z \rightarrow L^-L^+, Z \rightarrow L^-L^+,$ $Z \rightarrow \nu_\ell\bar{\nu}_\ell$

The cut efficiencies for signal and background at  $\sqrt{S}=500$  GeV are shown in Table 5. The bottom row is the total efficiency, which represents the ratio of the scattering cross-section size at Cut-2 to the scattering cross-section size at Basic cut. From the table we can see that the selected cuts suppress the background and take out the signal efficiently. After all the cuts, the total signal screening efficiency can reach 10.52%, while the total background screening efficiency can be reduced to 5.19% or even less. The integral brightness that can be excluded at  $m_{\tau'^\pm} = 180\text{GeV}, 200\text{GeV}, 220\text{GeV}$  and  $240\text{GeV}$  are  $3.0\text{ fb}^{-1}, 3.4\text{ fb}^{-1}, 4.9\text{ fb}^{-1}$  and  $14.9\text{ fb}^{-1}$  respectively. The required integral luminosities can be found to be  $18.1\text{ fb}^{-1}, 21.1\text{ fb}^{-1}, 30.9\text{ fb}^{-1}$  and  $94.3\text{ fb}^{-1}$  for  $m_{\tau'^\pm} = 180\text{GeV}, 200\text{Gev}, 220\text{Gev}$  and  $240\text{Gev}$ , respectively. The required integral luminosities increase with  $m_{\tau'^\pm}$ . This is mainly due to the fact that the signal cross-section decreases rapidly as  $m_{\tau'^\pm}$  increases, and at  $\sqrt{S}=500$  GeV the luminance rises sharply as it approaches the threshold  $m_{\tau'^\pm} = 250$  generated by the signaling

process. At the highest integrating luminance of  $4ab^{-1}$ , the  $m_{\tau^{\pm}}$  mass can be detected at 245 GeV.

Table 5 shows the cuts efficiency of signal and background at time  $\sqrt{S} = 1000 \text{GeV}$ . After all cuts, the total signal screening efficiency can reach 14.29%, while the total background screening efficiency can be reduced to 4.26% or even less. We can see that the integral luminosities that can be excluded at  $m_{\tau^{\pm}} = 250 \text{GeV}, 300 \text{GeV}, 350 \text{GeV}, 400 \text{GeV}$  and  $450 \text{GeV}$  are  $9.5 \text{fb}^{-1}, 9.6 \text{fb}^{-1}, 10.6 \text{fb}^{-1}, 12.8 \text{fb}^{-1}$  and  $23.1 \text{fb}^{-1}$ , respectively. The integral luminances that can be found at  $m_{\tau^{\pm}} = 250 \text{GeV}, 300 \text{GeV}, 350 \text{GeV}, 400 \text{GeV}$  and  $450 \text{GeV}$  are  $59.5 \text{fb}^{-1}, 59.7 \text{fb}^{-1}, 66.9 \text{fb}^{-1}, 79.8 \text{fb}^{-1}$  and  $144.2 \text{fb}^{-1}$  respectively. At  $\sqrt{S} = 1000 \text{GeV}$ , the luminance rises sharply as it approaches the threshold generated by the signaling process,  $m_{\tau^{\pm}} = 500 \text{ GeV}$ . At the highest integral brightness of  $8ab^{-1}$ , a mass of  $m_{\tau^{\pm}}$  can be detected at 475 GeV. Compared to the full hadronic channel, the purely leptonic process requires a much brighter integral brightness to exclude or discover VLLs. The exclusion and discovery of monomorphic VLLs and even Higgs through the full hadronic channel of the LC is much more efficient.

Table 5 Signal and background cut efficiency

Pure light	$\sqrt{s} = 500 \text{GeV}$	$\sqrt{s} = 1000 \text{GeV}$	$\sqrt{s} = 1500 \text{GeV}$
Basic cut	$\Delta R(x, y) > 0.4, p_T^{\ell, \tau} > 10 \text{GeV}, p_T^{b, j} > 20 \text{GeV},  \eta_{\ell, \tau, b}  < 2.5,  \eta_j  < 5.0$		
Trigger	$N(j) = 0, N(b) = 0, N(\tau) = 1, N(\ell) = 2$		
Cut-1	$\cancel{E}_T > 40 \text{GeV}$	$\cancel{E}_T > 50 \text{GeV}$	$\cancel{E}_T > 60 \text{GeV}$
Cut-2	$\Delta R(\tau_1, \ell_1) < 3.0$		

### 3.2 Exact Tests for Higgs Coupling on ILCs

$e^+e^- \rightarrow HZZ$  is an important process for probing Higgs self-coupling, and in this paper we test the extra dimensional effects of this process for different positive and negative electron polarization states, labeling this process as:

$$e^+(k_1, \lambda_1) + e^-(k_2, \lambda_2) \rightarrow H(p_1) + Z(p_2, \nu) + Z(p_3, \mu) \quad (16)$$

where  $k_i$  and  $p_i$  are the momentum of the initial and final state particles, respectively,  $3\lambda_i$  is the solenoidal degree of the positron, and  $\nu$  and  $\mu$  are the Lorentz indicators of the  $Z$  boson. The form of the Feynman diagram for the part of this process containing the graviton exchange effect is presented in Fig. 7.

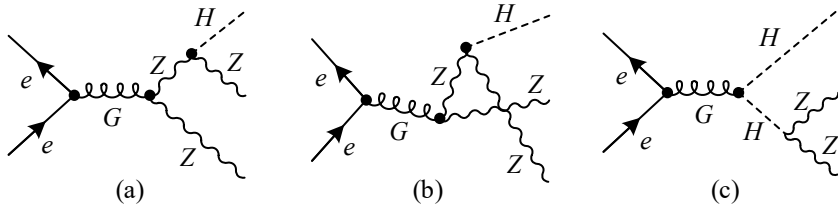


Figure 7  $e^+e^- \rightarrow HZZ$  progress

corresponding to the magnitude of each of the three plots above:

$$M_{(a)}^G(\lambda_1, \lambda_2) = \frac{gm_w D(s) P_{\rho\sigma\alpha\beta}}{2S_w C_w (m_H^2 + 2p_1 \cdot p_2)} \bar{v}(k_1, \lambda_1) [V_{eeG}]_{\rho\sigma} u(k_2, \lambda_2) [V_{ZZG}]_{\alpha\beta\mu\nu} \bar{v}(p_2)_\mu(p_3) \quad (17)$$

$$M_{(b)}^G(\lambda_1, \lambda_2) = M_{(a)}^G [(p_2, \nu) \leftrightarrow (p_3, \mu)] \quad (18)$$

$$M_{(c)}^G(\lambda_1, \lambda_2) = \frac{-gm_w D(s) P_{\rho\sigma\alpha\beta}}{2S_w C_w ((p_2 + p_3)^2 - m_H^2)} \bar{v}(k_1, \lambda_1) [V_{eeG}]_{\rho\sigma} (19) \\ u(k_2, \lambda_2) [V_{HHG}]_{\alpha\beta} g_{\mu\nu} \bar{v}(p_2)_\mu(p_3)$$

In the above equation  $s = (k_1 + k_2)^2$  is the center-of-mass system energy and  $D(s)$  is the propagator expression obtained by summing over  $KK$  excited states, see above:

$$D(s) = \frac{16\pi}{\kappa^2} M_s^{-4} \left( \frac{\sqrt{s}}{M_s} \right)^{n-2} \left[ \pi + 2iP \int_0^{M_s/\sqrt{s}} \frac{y^{n-1} dy}{1-y^2} \right] \quad (20)$$

In the above equation  $s = (k_1 + k_2)^2$  is the center-of-mass system energy and  $D(s)$  is the propagator expression obtained by summing over  $KK$  excited states with reference to the above equation:

$$D(s) = \frac{16\pi}{\kappa^2} M_s^{-4} \left( \frac{\sqrt{s}}{M_s} \right)^{n-2} \left[ \pi + 2iP \int_0^{M_s/\sqrt{s}} \frac{y^{n-1} dy}{1-y^2} \right] \quad (21)$$

The expression for  $P^{\mu\nu\alpha\beta}$  is as follows:

$$P^{\mu\nu\alpha\beta} = \eta^{\mu\alpha}\eta^{\nu\beta} + \eta^{\mu\beta}\eta^{\nu\alpha} - \frac{2}{n-2}\eta^{\mu\nu}\eta^{\alpha\beta} \quad (22)$$

where  $V_{eeG}, V_{ZZG}$  and  $V_{HHG}$  represent the vertices. The total magnitude of the process is obtained by adding the magnitude of the imaginary graviton exchange effect obtained above to the tree diagram order magnitude of the Standard Model section. For unpolarized colliding bundles, the total cross section can be obtained by the following equation:

$$\sigma_{LED}^{unpol.} = \frac{1}{2} \frac{1}{4|\vec{k}_1| \sqrt{s}} \int d\Phi_3 \frac{1}{4} \sum_{\lambda_1, \lambda_2} |M(\lambda_1, \lambda_2)|^2 \quad (23)$$

The first  $\frac{1}{2}$  factor in the above equation is due to the fact that the two  $Z$  bosons in the final state are all-identical particles. The representation of the phase space volume element for the three-body end-state process is given in the above equation. In the case of polarized colliding beams, the cross-section formula can be obtained by making the following substitution of the square of the matrix element in the above equation:

$$\begin{aligned} \sum_{\lambda_1, \lambda_2} |M(\lambda_1, \lambda_2)|^2 &\rightarrow \frac{(1+P_e)(1+P_p)}{2} |M(+,+)|^2 + \frac{(1+P_e)(1-P_p)}{2} |M(+,-)|^2 \\ &+ \frac{(1-P_e)(1+P_p)}{2} |M(-,+)|^2 + \frac{(1-P_e)(1-P_p)}{2} |M(-,-)|^2 \end{aligned} \quad (24)$$

where  $P_e \left( = \frac{N_e^+ - N_e^-}{N_e^+ + N_e^-} \right)$  and  $P_p \left( = \frac{N_p^+ - N_p^-}{N_p^+ + N_p^-} \right)$  are the polarizabilities of

electrons and positrons, respectively.

The calculations for the  $e^+ e^- \rightarrow HZZ$ -process were tested above to see if they were as expected. The polarization modes of positron and electron are denoted by + or -. The calculation process mentioned in 2.4 revealed that the cross section in the positive and negative modes is several times larger than the cross section in the negative and positive modes.

In Table 6, we list the  $3\sigma$ -exclusion limits and  $5\sigma$ -discovery limits for extra-dimensional effects when  $\sqrt{S}$  is some typical values, including both the cases of nonpolarized and +- polarized positron and negative electrons, where the masses of Higgs are taken to be  $m_h = 115\text{Gev}$  and  $180\text{ Gev}$ , respectively, and the polarizations of positron and negative electrons are taken to be  $P_p = 0.6$ ,  $P_p = 0.8$ , and the luminosity is taken to be  $L_{e^+e^-} = 500\text{fb}^{-1}$  in the calculations. From the table, we can see that the  $HZZ$  co-generation at the positron-negative collider is a good way of detecting the extra-dimensional effects in the a good generation channel. When  $\sqrt{S} = 3.5\text{ TeV}$ ,  $m_h = 115\text{Gev}$ , the maximum value of  $M_s$  is  $9.642$  and  $10.068\text{ TeV}$  for polarized and unpolarized colliders, respectively, and the exclusion limits of  $M_s$  are  $10.867$  and  $11.214\text{ TeV}$ , respectively, which shows that the extra-dimensional effects of the  $e^+ e^- \rightarrow HZZ$  process can be significantly improved by the linear collision beam with +-polarization.

Table 6 Higgs Self coupling effect

$m_H=115[\text{GeV}]$	$M_s[\text{GeV}]$			
$\sqrt{S} [\text{TeV}]$	Unpol.		Pol.+-	
	$3\sigma$	$5\sigma$	$3\sigma$	$5\sigma$
0.5	1920	1682	2028	1772
1.0	3485	3059	3652	3211
1.5	4917	4370	5126	4548
2.0	6372	5600	6621	5912
2.5	7851	7029	8126	7290
3.0	9345	8382	9652	8681

3.5	10876	9741	11213	10091
$m_H = 180 \text{ [GeV]}$	$M_s \text{ [GeV]}$			
$\sqrt{S} \text{ [TeV]}$	Unpol.		Pol.+ -	
	$3\sigma$	$5\sigma$	$3\sigma$	$5\sigma$
0.5	1610	1442	1712	1492
1.0	3355	3008	3451	3111
1.5	4857	4320	5024	4815
2.0	6312	5713	6539	5895
2.5	7862	7019	8026	7310
3.0	9372	8442	9632	8713
3.5	10896	9799	11220	10145

The  $5\sigma$  discovery limit and the  $3\sigma$  exclusion limit for extra-dimensional effects were tested in this case. For the  $e^+e^- \rightarrow HZZ$  process, when  $n=3, m_H = 115 \text{ GeV}, \sqrt{s} = 3.5 \text{ TeV}, M_s$  the  $5\sigma$  discovery limit is able to reach 9.75 TeV and 10.1 TeV for unpolarized and +- polarized (where  $P_{e^+} = 0.6, P_{e^-} = 0.8$ ), respectively.  $e^+e^-$  The accuracy of detecting extra dimensions will be greatly improved after positive and negative polarization of the beam current. Table 7 shows the Higgs particle coupling.

Table 7 Higg spolarization

$\sqrt{S} = 500 \text{ GeV ILC}$								
		Exhaust system ( $2\sigma$ )			Discovery ability ( $5\sigma$ )			
$\sqrt{S} = 500 \text{ GeV}$	ILC Pure light	Semilepton		Full hadron	Pure light	Semilepton		Full hadron
		Model A	Model B			Model A	Model B	
$m_{\tau'^{\pm}} (\text{GeV})$	[180,240]				[180,240]			
$L (\text{fb}^{-1})$	[3.0 14.9]	[0.4,2.0 ]	[1.0 3.5]	[0.1 0.3]	[18.1 94.3]	[2.6 12.4]	[6.1 21.9]	[0.9 1.7]

$\sqrt{S} = 1000 \text{GeV}$ ILC								
	Exhaust system ( $2\sigma$ )				Discovery ability ( $5\sigma$ )			
ILC $\sqrt{S} = 500 \text{GeV}$	Pure light	Semilepton		Full hadron	Pure light	Semilepton		Full hadron
		Model A	Model B			Model A	Model B	
$m_{\tau^\pm}(\text{GeV})$	[240,450]				[240,450]			
$L(\text{fb}^{-1})$	[9.9 23.2]	[1.4 4.4]	[4.8 11.3]	[0.3 0.4]	[61.8 144.2]	[8.8 26.4]	[30.3 76.9]	[1.9 1.7]

## 4. Conclusion

This paper discusses the discovery of the singlet vector lepton production mechanism and the self-coupling of Higgs on the ILC based on the ILC. The following conclusions are drawn from calculations and experiments:

(1) It is more efficient to exclude and find monomorphic VLLs and even Higgs through the full-strong subchannels of the LC. The integral luminosities that can be excluded at  $m_{\tau^\pm}=250 \text{V}, 300 \text{GeV}, 350 \text{GeV}, 400 \text{GeV}$  and  $450 \text{GeV}$  are  $9.5 \text{ fb}^{-1}, 9.6 \text{ fb}^{-1}, 10.6 \text{ fb}^{-1}, 12.8 \text{ fb}^{-1}$  and  $23.1 \text{ fb}^{-1}$ , respectively. Integral luminances of  $59.5 \text{ fb}^{-1}, 59.7 \text{ fb}^{-1}, 66.9 \text{ fb}^{-1}, 79.8 \text{ fb}^{-1}$ , and  $144.2 \text{ fb}^{-1}$  can be found at  $m_{\tau^\pm}=250 \text{ GeV}, 300 \text{ GeV}, 350 \text{ GeV}, 400 \text{ GeV}$ , and  $450 \text{ GeV}$ , respectively. At  $\sqrt{S} = 1000 \text{GeV}$ , the luminance rises sharply near the threshold generated by the signaling process,  $m_{\tau^\pm}=500 \text{ GeV}$ . At the highest integral brightness of  $8ab^{-1}$ , the  $m_{\tau^\pm}$  mass can be detected at 475 GeV. Compared to the full-strong subchannels, the purely light subchannel process requires a much brighter integral brightness to exclude or detect the VLL.

(2) +-polarized linear colliding beams can lead to a significant increase in the extra-dimensional effects of the  $e^+e^- \rightarrow HZZ$ -process. Combined HZZ generation on a positron collider is a good generation channel for detecting extra-dimensional effects. When  $\sqrt{S}=3.5 \text{ TeV}$ ,  $m_h=115 \text{ GeV}$  the collider can detect  $M_S$  values up to 9.642

TeV and 10.068 TeV for polarized and unpolarized, respectively, while the 4 exclusion limits are 10.867 TeV and 11.214 TeV, respectively.

## About the Author

Wenrong Sun now study at School of Science. The Hong Kong University of Science and Technology, major in Physics.

## References

- [1] Wolk, B. J. . (2020). The underlying geometry of the cam gauge model of the standard model of particle physics. International Journal of Modern Physics A, 35(7), 2050037.
- [2] Mariotti, C. , & Passarino, G. . (2017). Higgs boson couplings: measurements and theoretical interpretation. International Journal of Modern Physics A, 32(04), 321-154.
- [3] Poh, Z. , & Raby, S. . (2017). Vector-like leptons: muon g-2 anomaly, lepton flavor violation, higgs\ln, decays, and lepton non-universality. Physical Review D, 96.
- [4] Shrihari, G. , & Subhra, M. T. . (2017). Gauge singlet vector-like fermion dark matter, lhc diphoton rate and direct detection. Advances in High Energy Physics, 2017, 1-14.
- [5] Ezquiaga, Jose María, García-Bellido, Juan, & Morales, E. R. . (2017). Primordial black hole production in critical higgs inflation. Physics Letters B, S0370269317309310.
- [6] Zhao, & Jun. (2018). The higgs properties in the mssm after the lhc run-2. International Journal of Modern Physics A, 1841001.
- [7] Yang, B. , Li, J. , Wang, M. , & Shang, L. . (2021). Search for the singlet vectorlike lepton in semileptonic channel at future  $e^+ e^-$  colliders. Physical review, D.
- [8] Shang, L. , Wang, M. , Heng, Z. , & Yang, B. . (2021). Search for the singlet vector-like lepton at future  $e^+ e^-$  colliders. The European Physical Journal C(5).
- [9] Das, P. , Das, M. K. , & Khan, N. . (2021). A new feasible dark matter region in the singlet scalar scotogenic model. Nuclear Physics B, 964(5), 115307.

- [10] Bhattacharya, S. , Sahoo, N. , & Sahu, N. . (2017). Singlet-doublet fermionic dark matter, neutrino mass and collider signatures. *Physical Review D*, 96(3).
- [11] Chang, J. , Cheung, K. , Lee, J. S. , & Park, J. . (2020). Probing the trilinear higgs boson self-coupling at the high-luminosity lhc via multivariate analysis. *Physical Review D*, 101.
- [12] Arganda, E. , Garcia-Garcia, C. , & Herrero, M. J. . (2019). Probing the higgs self-coupling through double higgs production in vector boson scattering at the lhc. *Nuclear Physics B*, 945, 114687.
- [13] Braathen, J. , & Kanemura, S. . (2019). Leading two-loop corrections to the higgs boson self-couplings in models with extended scalar sectors. *Physics Letters B*, 796, 38-46.